AIP Advances

Generative adversarial networks with physical evaluators for spray simulation of pintle injector

Cite as: AIP Advances **11**, 075007 (2021); https://doi.org/10.1063/5.0056549
Submitted: 11 May 2021 • Accepted: 10 June 2021 • Published Online: 02 July 2021

Hao Ma, Botao Zhang, Chi Zhang, et al.

Generative adversarial networks with physical evaluators for spray simulation of pintle injector

Cite as: AIP Advances 11, 075007 (2021); doi: 10.1063/5.0056549
Submitted: 11 May 2021 • Accepted: 10 June 2021 •
Published Online: 2 July 2021

Hao Ma,[1,a] Botao Zhang,[2] Chi Zhang,[3] and Oskar J. Haidn[1]

AFFILIATIONS

[1] Department of Aerospace and Geodesy, Technical University of Munich, 85748 Garching, Germany
[2] Key Laboratory for Liquid Rocket Engine Technology, Xi'an Aerospace Propulsion Institute, 710100 Xi'an, China
[3] Department of Mechanical Engineering, Technical University of Munich, 85748 Garching, Germany

[a] Author to whom correspondence should be addressed: hao.ma@tum.de

ABSTRACT

Due to the adjustable geometry, pintle injectors are especially suitable for liquid rocket engines, which require a widely throttleable range. However, applying the conventional computational fluid dynamics approaches to simulate the complex spray phenomenon in the whole range still remains a great challenge. In this paper, a novel deep learning approach used to simulate instantaneous spray fields under continuous operating conditions is explored. Based on one specific type of neural network and the idea of physics constraint, a *Generative Adversarial Networks with Physics Evaluators* framework is proposed. The geometry design and mass flux information are embedded as inputs. After the adversarial training between the generator and discriminator, the generated field solutions are fed into two physics evaluators. In this framework, a mass conversation evaluator is designed to improve the training robustness and convergence. A spray angle evaluator, which is composed of a down-sampling *Convolutional Neural Network* and theoretical model, guides the networks to generate the spray solutions more closely according to the injection conditions. The characterization of the simulated spray, including the spray morphology, droplet distribution, and spray angle, is well predicted. This work suggests great potential for prior physics knowledge employment in the simulation of instantaneous flow fields.

I. INTRODUCTION

Due to their wider throttling range and greater combustion stability, pintle injectors are especially suitable for liquid rocket engines that require deep, fast, and safe throttling,[1–3] such as the descent propulsion system in the Apollo program[4] and the reusable Merlin engine of SpaceX.[5]

In practical throttleable engine applications, the pintle is movable to alter the injection area so that the mass flow rate of the injected propellants can be varied continuously according to the economical and safe thrust curve in a given situation.[6] However, in the previous spray simulations of pintle injectors, the changes were only considered under discrete condition combinations over a limited number of select operating points.[7–9] For the traditional discrete methods they used, simulations have to be conducted repeatedly to vary the operating conditions and the computational cost becomes prohibitively expensive.[10] Innovations for the spray simulation of the pintle injector are needed to address this issue.

Contrarily, the machine learning approach, especially the *Neural Network* (NN), has demonstrated its efficiency to predict the flow fields under different conditions with a single surrogate model.[11,12] Previous research studies on flow field prediction using the NN are mainly focused on the data-driven method. In addition to the indirect way using the closure model,[13,14] the field solution can also be directly obtained from the network model, which is trained with a large number of samples.[15–18] However, some predictive results obtained by data-driven methods may still exhibit considerable errors against physics laws or operating conditions.[19–21] In addition, in some sparse data regimes, some machine learning techniques lack robustness and fail to provide guarantees of convergence.[22] For the purpose of remedying the above-mentioned shortcomings of data-driven methods, the physics-driven/informed methods are proposed recently.[23,24] By providing physics information, NNs are

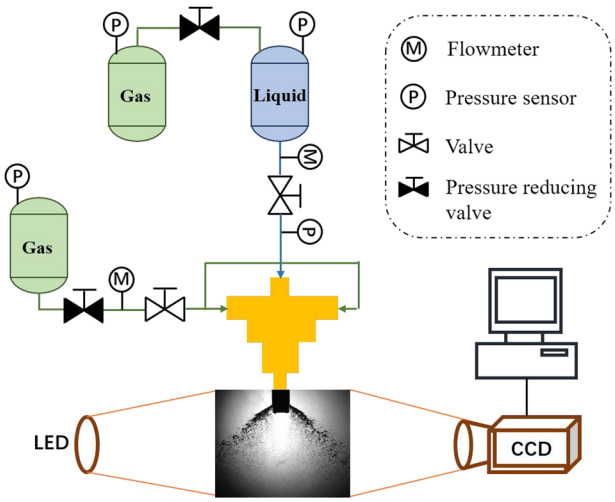

FIG. 1. Schematic of the experimental facilities. The test bench is composed of a gas–liquid pintle injector, a propellant feed system, and a control system. The spray visualization system includes a LED lamp and a high-speed camera.

able to directly obtain field solutions that obey physical laws and operating conditions.[25] In these works, *Partial Differential Equations* (PDEs) were employed in the loss function to explicitly constrain the network training.[26,27]

In the state-of-the-art neural network methods, *Generative Adversarial Networks* (GANs) proposed by Goodfellow *et al.*[28] are efficient to generate the instantaneous flow fields.[29,30] Despite the impressive performance for unsupervised learning tasks, the quality of generated solutions by GANs is still limited for some realistic tasks.[31] In addition, as shown in the training results later, the transient nature of the spray injection and liquid sheet break results in the extreme difficulty of usual networks to qualify the place and intensity of dominating characterizations.

In this paper, based on one specific type of GAN and the idea of physics constraint, a novel *Generative Adversarial Networks with Physical Evaluators* (GAN-PE) framework is proposed. By introducing mass conversation and spray angle models as the two evaluators, this framework has a better training convergence and predictive accuracy. The trained model is able to simulate the macroscopic morphology and characterization of the instantaneous flow fields under different conditions. This paper is organized as follows: We first introduce the experimental settings and dataset acquisition. Second, the architecture of GAN-PE and the detailed parts are described. Then, the learning results of numerical experiments are presented for validation. Finally, conclusions are drawn.

II. DATASET FROM EXPERIMENTS

Our training data are extracted from the spray experimental results of the pintle injectors.

A. Experimental facilities

The non-reactive cold experiments were conducted at atmospheric pressure. The dry air is used for axial flows and filtered water for radial flows. The schematic of experimental facilities is shown in Fig. 1. A back-lighting photography technique is used for instantaneous spray image visualization. The image acquisition system consists of a *light-emitting diode* (LED) light source, a high-speed camera, and a computer. The exposure time is 10 μs, and the frame rate is 50k fps.

The detailed gas–liquid pintle injector is shown in Fig. 2. In order to study the influence of the momentum ratio on the spray angle, the experimental device is designed to use the replaceable parts. In the experiment, the height of the radial liquid jet outlet L_{open} and the thickness of the axial gas sheet T_{gs} are adjusted by changing the height of the sleeve and the axial gap distance, respectively. When the liquid propellant is injected radially from the two sides of the pintle end through the manifold, the liquid columns are formed. These columns are broken by the axial gas propellant injection from the gap cling to the pintle. Finally, due to impingement and collision, the liquid columns break and form a plane conical spray like a hollow-cone atomizer. This design induces vigorous mixing of the gaseous and liquid propellants, which yields a high combustion efficiency.[32]

B. Dataset acquisition

The spray experiments are carried out with the throttling level L_t of 40%–80%. L_t is varied by the linear adjustment of the height of the radial liquid jet outlet and the thickness of the axial gas sheet. The radial liquid jet outlet heights at throttling levels of 40%, 60%,

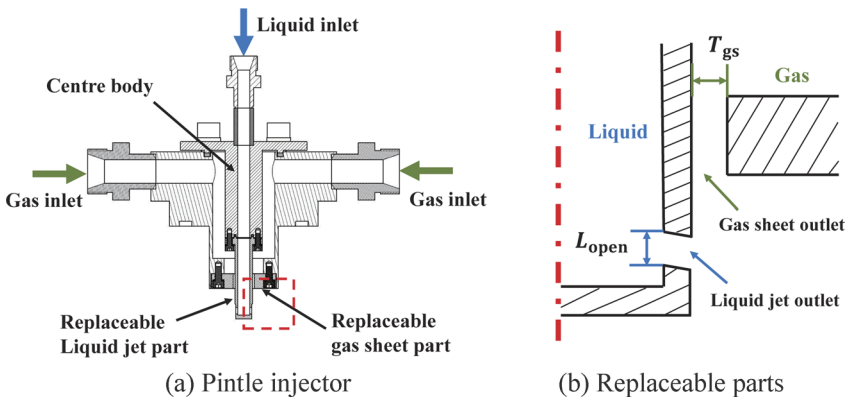

FIG. 2. Gas–liquid pintle injector. (a) Pintle injector within manifolds. The experimental injector consists of a gas manifold, a replaceable liquid manifold, a replaceable axial gas sheet adjustment annular, a central cylinder, and a sleeve. (b) Schematic of the replaceable parts in the red square of (a). In order to facilitate the optical observation about the spray angle, two symmetrical radial liquid jet orifices are designed on the replaceable central cylinder. L_{open} and T_{gs} are the injector opening distance and gas sheet thickness, respectively.

TABLE I. Experimental operating conditions. m_g and m_l are the mass flow rate of gaseous and liquid propellants, respectively. C_{TMR} is the momentum ratio of the two propellants.

L_t (%)	L_{open} (mm)	T_{gs} (mm)	m_g (g/s)	m_l (g/s)	C_{TMR}
80	4.0	4.0	22.17	18.55–40.54	1.01–4.92
60	3.0	3.0	15.70	14.85–30.46	1.22–5.14
40	2.0	2.0	9.85	8.85–20.45	0.98–5.21

and 80% are 2, 3, and 4, respectively. When L_t is fixed, the height of the radial liquid jet outlet is fixed and equal to the thickness of the axial gas sheet. Table I shows the operating conditions of the experimental campaign and the corresponding key specifications of the pintle injector. The temperature of the liquid and gas is 298.15 K. The mass flow rate m_l is determined by the variation of liquid pressure upstream. Eventually, 35k raw images were captured and 29k of them were used for training and the others for validation.

As shown in Fig. 3, to measure the spray angle, the spray images obtained in the experiment are post-processed to clarify the spray boundary. The average of ten images with the same time interval is used to measure the spray angle manually. Every operation condition has 1k raw images, so the 100th, 200th, . . ., 900th, and 1000th images are averaged. Then, the spray angles of the time-averaged spray images, defined as $\theta = \frac{1}{2}(\theta_1 + \theta_2)$, are manually measured. Since the raw images are all captured in the steady injection stage and no temporal fluctuations, the measured angle value is unique per operating condition. Note that the average images and the corresponding manually measured angles are only used to train the spray angle estimator, i.e., the down-sampling CNN in the spray angle evaluator. The raw images are used in the training of GAN-PE.

The resolutions of the instantaneous spray image are 640 × 480. In order to reduce the training cost, the images are interpolated to the images with a resolution of 128 × 128. While the measured angle values, which represented the nature of the spray phenomenon, are fixed despite the image scaling.

III. METHODOLOGY

A. Overview

Here, a *Generative Adversarial Networks with Physical Evaluators* (GAN-PE) framework is proposed. As shown in Fig. 4, the GAN-PE is composed of four parts: *generator* (*G*), *discriminator* (*D*), and two physical evaluators. The field solutions are generated by *G*, and the other three parts are employed to guarantee that the outputs catch the spray morphology and obey the operating conditions. The GAN is the base of the proposed network framework; the *G* captures the real spray data distribution, which corresponds to the operation conditions; and the *D* estimates the probability that a condition–sample pair came from the training data rather than *G*. There are also two evaluators designed to improve the performance of GANs. The first evaluator, *Mass Conservation Evaluator* (E_{MC}), is used to improve the generation robustness by calculating the ring error between output and the corresponding average target. The second evaluator, *spray angle evaluator* (E_{SA}), is used to improve the predictive accuracy in the specific operating conditions by comparing the output angle with the theoretical one. Fed with the outputs from *G*, the losses of *D*, E_{MC}, and E_{SA} are calculated, respectively. After that, backpropagation is applied to adjust the U-net *Convolutional Neural Network* (CNN) of *G* to generate a new spray field that more satisfies the conditions and prior physics knowledge. After enough iterations, the network will be able to generate a "correct" spray field.

B. GAN

1. Generator

From inputs toward outputs, the network of *G* consists of two parts: encoding and decoding.[33] In the encoding process, the

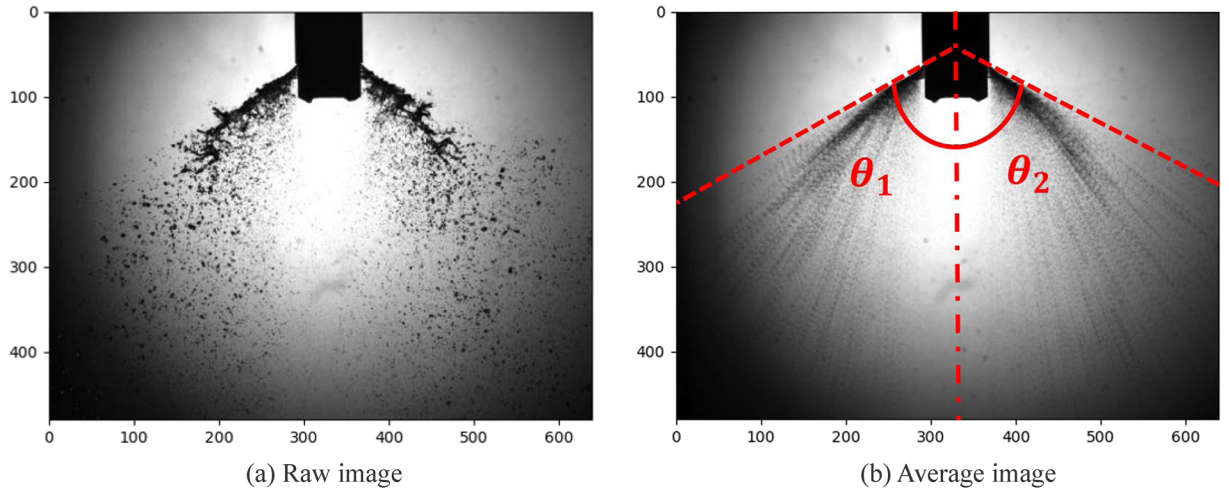

FIG. 3. Data acquisition. The resolution of the images is 640 × 480. The raw monochrome pictures are processed as 8-bit gray images in which every pixel has a gray value and the range is 0–255. The average is obtained by calculating the mean gray value of raw images. The images are regarded as the 2D matrices whose dimensions are 640 × 480.

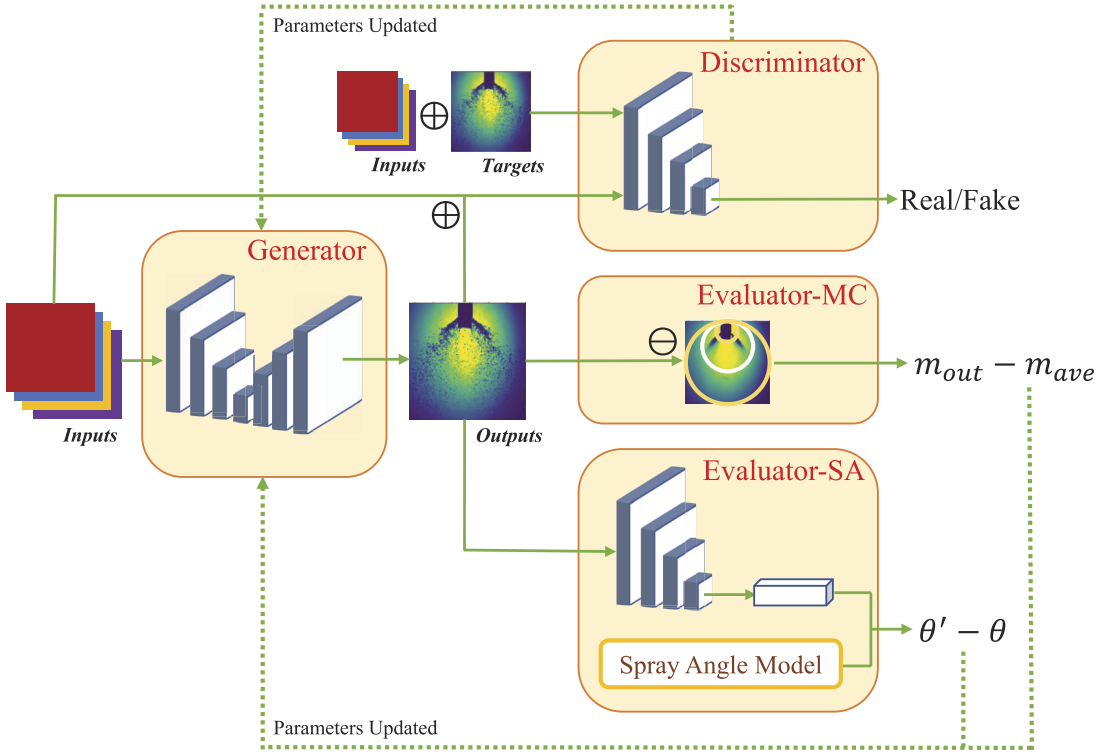

FIG. 4. Schematic of the proposed network framework. Fed with the operating conditions, the U-net generator outputs a field solution of the spray. The discriminator, mass conservation, and spray angle losses are utilized to update the generator by backpropagation.

operating conditions L_{open}, T_{gs}, m_{g}, and m_{l} are resized as four feature channels of the input tensor for convolutional down-sampling with corresponding kernels.[34,35] After that, the matrices with a size of 128 × 128 are progressively reduced to 512 single-value vectors. Each layer of the network consists of a convolution operation, batch normalization, and a non-linear activation function. By the convolutional calculation, along with the increasing number of feature channels, the matrix size is down-sampled by a factor of 2. In this way, the information of operating conditions is translated into the extracted features in the next layer. In addition, skip-concatenations from input to output feature channels are introduced to ensure that operating condition information is available in the following up-sampling process for inferring the solution. Then, the decoding part works in an opposite way, which can be regarded as an inverse convolutional process mirroring the behavior of the encoding part. Along with the increase in spatial resolution, the spray fields are reconstructed based on the single-value vectors by up-sampling operations. For more details of the U-net architecture and convolutional block, including active function, pooling, and dropout, see Ref. 27.

The weighted loss function considering the following discriminator and evaluators is written as

$$\mathscr{L}(D, E_{\text{MC}}, E_{\text{SA}}) = \mathscr{L}_D + \alpha \mathscr{L}_{E_{\text{MC}}} + \beta \mathscr{L}_{E_{\text{SA}}}, \tag{1}$$

where $\mathscr{L}_D$, $\mathscr{L}_{E_{\text{MC}}}$, and $\mathscr{L}_{E_{\text{SA}}}$ are the loss terms that are calculated by D, E_{MC}, and E_{SA}, respectively. In addition, α and β are the constant hyperparameters that are manually tuned before training to adapt the scales of these loss terms. Here, the orders of magnitude of α and β are 2 and 1, respectively. After proper training, both generator and discriminator losses remain stable and the generator is able to map a spray sample from a random distribution to the desired one that obeys the physical knowledge and conditions.

2. Discriminator

The discriminator in a GAN is simply a classifier. It tries to distinguish real samples from the data created by the generator, i.e., fake data. The discriminator's training data come from two sources. One consists of the real data instances, here are the real experimental images. D uses these instances as positive examples during training. The other are the fake data instances created by the generator. The discriminator uses these instances as negative examples during training. Then, D is used to feed the possibility that samples come from the targets rather than generation distribution back to G. We use *Least Squares Generative Adversarial Networks* (LSGANs) settings to train the D and the G simultaneously.[36] This special type of GAN helps to remedy the gradient vanishing by using the least squares loss function instead of the sigmoid cross entropy loss function.[37]

Here, D is modified by the encoder of the G, which means that the generating solutions from G are down-sampled by the re-convolutional calculation so that the spray field information is concluded into the linear 1D tensor. Then, this 1D tensor will be used to

be trained to maximize the probability of assigning the correct label, real or fake, to both training targets and generating solutions. Similar to the work in Ref. 38, we use the input–output and input–target pairs to feed D instead of only output and target in the random image generation tasks. The operating conditions and the outputs/targets are concatenated as the different feature channels in a 4D data tensor. In this way, D not only discriminates between the real and fake but also helps to judge whether the outputs accord with the corresponding conditions.

The loss functions for LSGANs are defined as

$$\begin{aligned}\min_D V_{\mathrm{GAN}}(D) &= \frac{1}{2}\mathbb{E}_{\boldsymbol{x}\sim p_{data}(\boldsymbol{x})}[(D(\boldsymbol{x})-b)^2] \\ &\quad + \frac{1}{2}\mathbb{E}_{\boldsymbol{z}\sim p_z(\boldsymbol{z})}[(D(G(\boldsymbol{z}))-a)^2], \\ \min_G V_{\mathrm{GAN}}(G) &= \frac{1}{2}\mathbb{E}_{\boldsymbol{z}\sim p_z(\boldsymbol{z})}[(D(G(\boldsymbol{z}))-c)^2],\end{aligned} \tag{2}$$

where $\boldsymbol{x}$ is the training data and $\boldsymbol{z}$ is the input variables. In addition, a and b are the labels for fake data and real data, respectively; and c denotes the value that G wants D to believe for the generated solutions. Here, we apply $a = 0$ and $b = c = 1$. Therefore, $\mathscr{L}_D$ is equal to the second part of Eq. (2).

C. Evaluators

1. Mass conservation evaluator

As shown in Fig. 5, we assume that there are a few spherical volumes with different diameters that are tangent at the middle point of the upper boundary in both generating images and the average images. The idea originates from that the spray phenomenon obeys the mass conservation law. Because the propellants are injected from the two flanks of the central pintle and the width of the image's normal direction is fixed, the 3D effect is ignored and the spheres are simplified to the 2D rings. The mass fluxes of droplets through one specific ring in every instantaneous frame are equivalent. The spray field generation is indeed a 2D image reconstruction task. Therefore, the "mass" here is a broader concept, which also involves the background shadow, i.e., the quasi-mass in one position is represented by the gray value of the corresponding pixel. Following the definition of "L1loss" that is widely used in the machine learning community, we define a mass conservation loss here. The difference is that the former measures the sum of absolute errors between each element in the generation and target,[39] but ours first calculates a gray value summation of every element in one concerning ring and then compares absolute error between the corresponding rings in the generation and target and, at last, the summation of the errors.

The mass conservation error, i.e., the loss term from E_{MC}, is defined as

$$\mathscr{L}_{E_{\mathrm{MC}}} = \begin{cases} \sum_{k=1}^{m}\left|\sum_{i=1}^{n} x_i - \sum_{j=1}^{n} y_j\right|_k, & \mathscr{E} \geq \mathscr{E}_{\mathrm{thr}}, \\ 0, & \mathscr{E} < \mathscr{E}_{\mathrm{thr}}, \end{cases} \tag{3}$$

where x and y are the gray values in generated images and average targets, respectively. In addition, m is the number of concerning rings and n is the number of data points in one concerning ring in the matrix. $\mathscr{E}$ is the error between the output and average matrix and defined as

$$\mathscr{E} = \sum_{i=1}^{N}|x_i - y_i|, \tag{4}$$

where N is the number of all the data points in the matrix. To improve the generation randomness and in view of the error caused

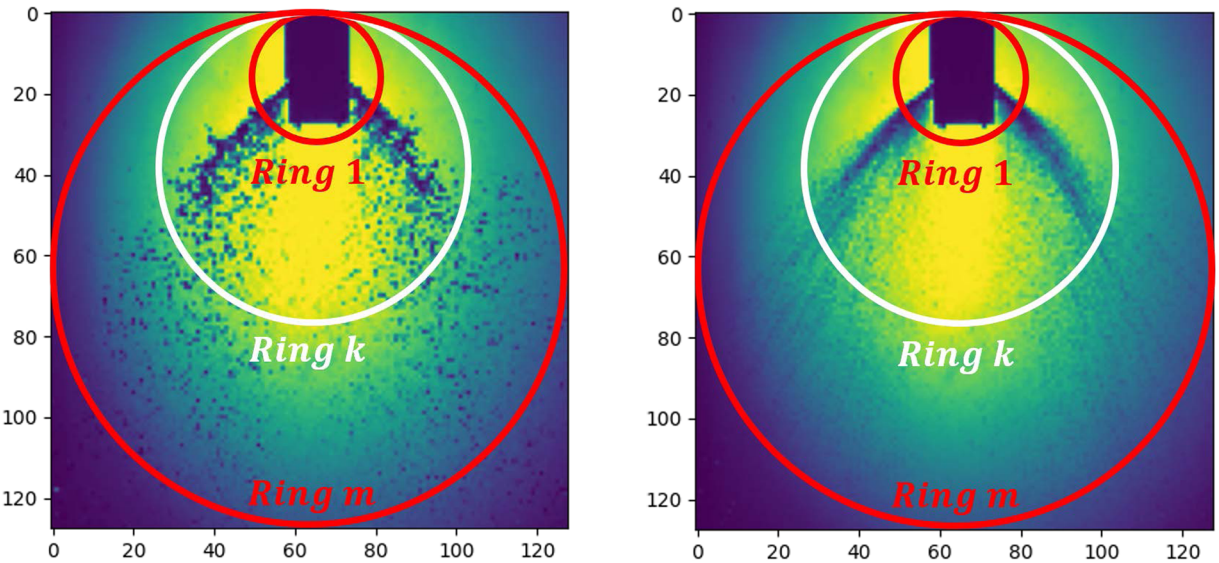

(a) Generated images (b) Average target

FIG. 5. Mass conservation. The resolution of the images is 128 × 128. The rings remain tangent at the central point of the top edge.

by light transmission and reflection, the loss threshold $\mathscr{E}_{thr}$ is introduced herein. Once the loss is less than the threshold, this loss term will be ignored.

2. Spray angle evaluator

The present evaluator is composed of two parts: one is the theoretical model of the spray angle and the other is a CNN encoder to estimate the spray angles from the generated field solutions.

The schematic diagram of the theoretical model of the spray angle is shown in Fig. 6. Several basic hypotheses must be declared before carrying out the theoretical analysis: (a) An element of fluid emerging from the jet exit is assumed to have the constant length and width equal to the jet exit length L_{open} and width W, as it moves along the trajectory; (b) liquid jet deformation, evaporation, and droplet dispersion are ignored; (c) the fluid element has a constant y-component velocity and an initial angle equal to the central propellant deflection angle φ; (d) the spray angle is assumed to be equal to the slope of the liquid jet at the position where it passes through the gas film; and (e) surface tension, gravity, friction, heat transfer, and phase change are ignored.

Following the definition in Ref. 40, the aerodynamic drag F_d of the liquid element in the x-direction is

$$F_d = \frac{1}{2} C_d \rho_g (v_g - v_l \cos\varphi)^2 WH, \tag{5}$$

where C_d is the drag coefficient. v_g and v_l are the gas velocity and initial liquid element velocity, respectively. According to Newton's second law in the x-direction, there is

$$\frac{1}{2} C_d \rho_g (v_g - v_l \cos\varphi)^2 WH = m_l a = \rho_l W L_{open} H \frac{dv_x}{dt}, \tag{6}$$

where m_l and a are the mass and acceleration of the liquid element, respectively. v_x is the x-component of the liquid element velocity. It

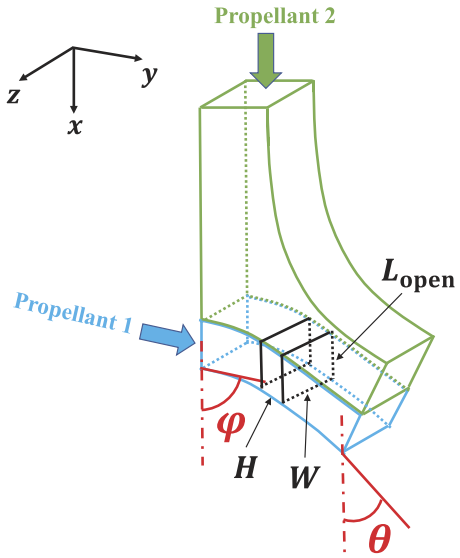

FIG. 6. Schematic of the spray angle model. L_{open} and W are the length and width of the radical rectangular section, respectively. H is the axial height of the liquid element.

can be rewritten as

$$\frac{dv_x}{dt} = \frac{C_d}{2} \frac{\rho_g}{\rho_l} \frac{(v_g - v_l \cos\varphi)^2}{L_{open}}. \tag{7}$$

Then, the integration of Eq. (7) with respect to time is

$$\int_0^t \frac{dv_x}{dt} dt = \int_0^t \frac{C_d}{2} \frac{\rho_g}{\rho_l} \frac{(v_g - v_l \cos\varphi)^2}{L_{open}} dt, \tag{8}$$

and then,

$$v_x|_0^t = \frac{C_d}{2} \frac{\rho_g}{\rho_l} \frac{(v_g - v_l \cos\varphi)^2}{L_{open}} t. \tag{9}$$

Since $v_x(0) = v_l \cos\varphi$, there is

$$v_x = \frac{C_d}{2} \frac{\rho_g}{\rho_l} \frac{(v_g - v_l \cos\varphi)^2}{L_{open}} t + v_l \cos\varphi. \tag{10}$$

As $v_x = dx/dt$, the integration with respect to time is

$$x = \frac{C_d}{4} \frac{\rho_g}{\rho_l} \frac{(v_g - v_l \cos\varphi)^2}{L_{open}} t^2 + v_l \cos\varphi t, \tag{11}$$

where x is the x-coordinate of the element's trajectory. Since the y-component velocity remains constant and $v_y = v_l \sin\varphi = y/t$, where y is the y-coordinate, the mathematical expression of the element trajectory is derived as

$$x = \frac{C_d}{4} \frac{\rho_g}{\rho_l} \frac{(v_g - v_l \cos\varphi)^2}{L_{open}} \left(\frac{y}{v_l \sin\varphi} \right)^2 + \frac{v_l \cos\varphi y}{v_l \sin\varphi}. \tag{12}$$

For the collision between the gas sheet and the rectangular liquid jet, the momentum ratio is

$$C_{TMR} = \frac{\dot{m}_l v_l}{\dot{m}_g v_g} = \frac{\rho_l v_l^2 A_l}{\rho_g v_g^2 A_g} = \frac{\rho_l v_l^2 W L_{open}}{\rho_g v_g^2 WH} = \frac{\rho_l v_l^2 L_{open}}{\rho_g v_g^2 H}. \tag{13}$$

Therefore, Eq. (12) is expressed in terms of the momentum ratio C_{TMR} as follows:

$$x = \frac{C_d}{4 C_{TMR} H \sin^2\varphi} \left(1 - \frac{v_l \cos\varphi}{v_g} \right)^2 y^2 + \frac{\cos\varphi}{\sin\varphi} y. \tag{14}$$

At the position of penetrating through the gas sheet where $y = H$, the trajectory expression is modified to

$$x = \left[\frac{C_d}{4 C_{TMR} \sin^2\varphi} \left(1 - \frac{v_l \cos\varphi}{v_g} \right)^2 + \frac{\cos\varphi}{\sin\varphi} \right] y, \tag{15}$$

and the slope of the liquid jet θ is obtained as

$$\theta = 90^\circ - \arctan\left[\frac{C_d}{4 C_{TMR} \sin^2\varphi} \left(1 - \frac{v_l \cos\varphi}{v_g} \right)^2 + \frac{\cos\varphi}{\sin\varphi} \right]. \tag{16}$$

The theoretical model assumes that the liquid jet does not deform, but in reality, it will deform under aerodynamic forces, which results in a reduction of the effective momentum of the

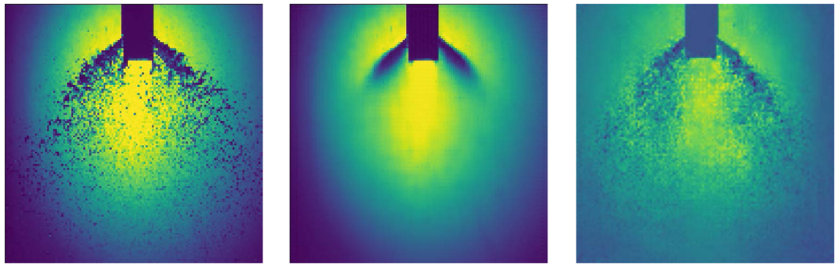

FIG. 7. Comparison of the CNN generator and original GAN. The operating condition is $L_{open} = T_{gs} = 4$ mm, $m_l = 35.81$ g/s, and $m_g = 22.17$ g/s.

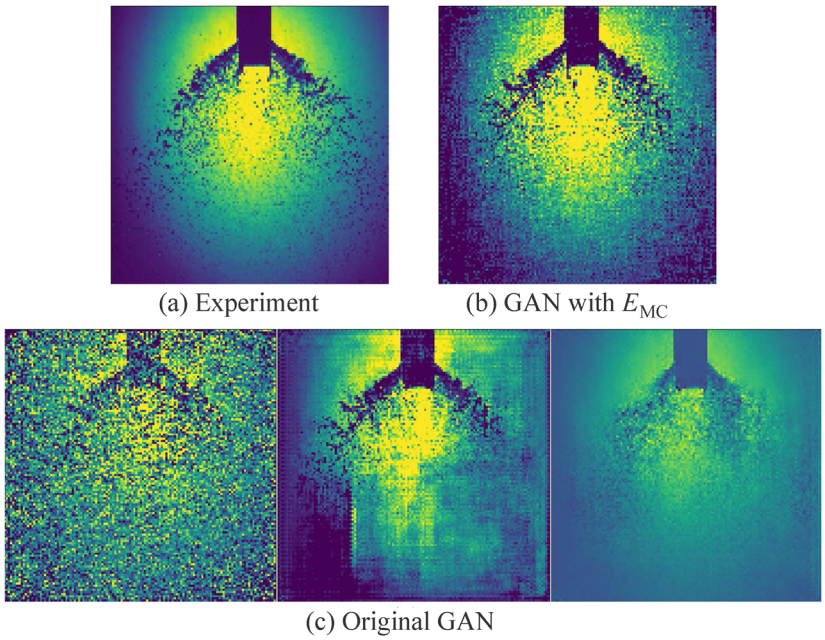

FIG. 8. The comparison between the results of with or without E_{MC}. Compared with the results without E_{MC}, GAN with E_{MC} has a clearer and more regularizing reconstruction of the spray field.

TABLE II. Spray angle estimation by the manual measurement and CNN.

	L_t = 80%			L_t = 60%			L_t = 40%		
C_{TMR}	MM	CNN	Error (%)	MM	CNN	Error (%)	MM	CNN	Error (%)
0.52–0.56	31.27	29.70	5.0	29.31	28.04	4.3	26.05	27.57	5.8
0.79–0.86	36.32	35.10	3.4	33.12	34.54	4.3	31.59	32.61	3.2
0.98–1.22	40.67	41.98	3.2	34.89	35.60	2.0	34.67	35.15	1.4
1.29–1.34	41.98	40.37	−3.8	39.21	39.34	0.3	36.36	37.0	1.75
1.50–1.70	44.37	45.99	3.7	42.87	43.37	1.2	39.43	38.08	−3.4
1.98–2.04	45.28	47.45	4.8	43.43	44.62	2.7	41.01	41.47	1.1
2.56–2.69	49.88	49.43	−0.9	47.34	45.46	−4.0	44.64	44.39	−0.6
2.90–3.22	50.36	50.02	−0.7	48.13	47.07	−2.2	44.98	45.64	1.5
3.33–3.39	51.32	52.92	3.1	48.12	48.75	1.3	46.01	46.64	1.4
3.83–4.12	52.18	52.55	0.7	48.84	51.09	4.6	47.64	48.98	2.8
4.50–4.88	54.39	53.92	−0.9	49.34	50.57	2.5	48.80	49.60	1.7
5.12	54.55	55.96	2.6	49.41	50.75	2.7	⋯	⋯	⋯

liquid jet. Consequently, the liquid jet deformation factor γ, which is obtained through the experimental results, is introduced to modify the spray angle theoretical model. In this way, Eq. (16) is modified to

$$\theta = \gamma\left\{90^\circ - \arctan\left[\frac{C_d}{4C_{TMR}\sin^2\varphi}\left(1 - \frac{v_l\cos\varphi}{v_g}\right)^2 + \frac{\cos\varphi}{\sin\varphi}\right]\right\}. \quad (17)$$

Note that the spray angle model derived above has been demonstrated by the experimental results. In fact, when there is no central propellant deflection and $\varphi = 90^\circ$, Eq. (17) could be simplified as $\theta = \gamma[90^\circ - \arctan(C_d/4C_{TMR})]$. It formally corresponds to the experimental fitting model $\theta = C_1 \arctan(C_2 C_{TMR})$ of the liquid–liquid pintle injector in Ref. 41, where C_1 and C_2 are the fitting parameters.

In the field of medical image analysis, the machine learning approach, especially the deep neural networks, has been employed for automated scoliosis assessment.[42–44] In these publications, the x-ray images are fed into the neural network estimator and the spinal Cobb angles are obtained. Similarly, inside the E_{SA}, there is a well-trained spray angle estimator to output the angle values from the predictive images. The architecture of this down-sampling CNN is like D, except the addition of one fully connected layer in the end to output the estimated spray angle θ'.

The loss term from E_{SA} is calculated as

$$\mathscr{L}_{E_{SA}} = |\theta' - \theta|. \quad (18)$$

IV. RESULTS

A. Model validation

Figure 7 shows the generated results in one typical operating condition of the CNN generator and original GAN, which consist of only G and D. The L1 loss used by the CNN generator compares the difference between the generations and targets. This absolute error loss performs very well in some steady or mean state field prediction tasks, such as the work in Refs. 21 and 27. However, when the training cases have a multi-modal distribution, this loss will fail. In our spray field prediction task, although the morphology under one specific operating condition is similar, the detailed droplets are distinguishable. Therefore, the instantaneous spray field solution has many possibilities, which are like the various frames at different times. However, the L1 loss averages all the possibilities and produces a very blurry average image instead. However, the discriminator in GANs, which can be regarded as the loss of generator, is not an explicit loss function. Instead of the pixel-wise loss, D is an approximation loss, which discriminates between the real and fake data distributions and guides the spray generation with detailed morphology.

However, in the training process of GANs, the generator and discriminator have to be balanced trained and the convergence is often an unstable state. The discriminator and generator are always in a seesaw battle to undercut each other. Similar to the work in Ref. 45, we maintain a dynamic ratio between the number of gradient descent iterations on the discriminator and the generator using *Exponential Moving Average* (EMA).

For the spray simulation task, the discriminator has difficulties capturing the detailed feature of the small droplets. The $\mathscr{L}_D$ has a possibility of becoming less meaningful through the training process. G will update itself based on the random feedback and the quality of generation may collapse. The G outputs low-quality images through many epochs, and some of them show faint spray patterns in the background but are easily identified as fake. It will be very easy for the discriminator to distinguish the targets and generation so the values of the loss from D drop to zero rapidly.

The comparison of generated spray images from different frameworks demonstrates the superior performance of the mass conservation evaluator as shown in Fig. 8. In some generated images,

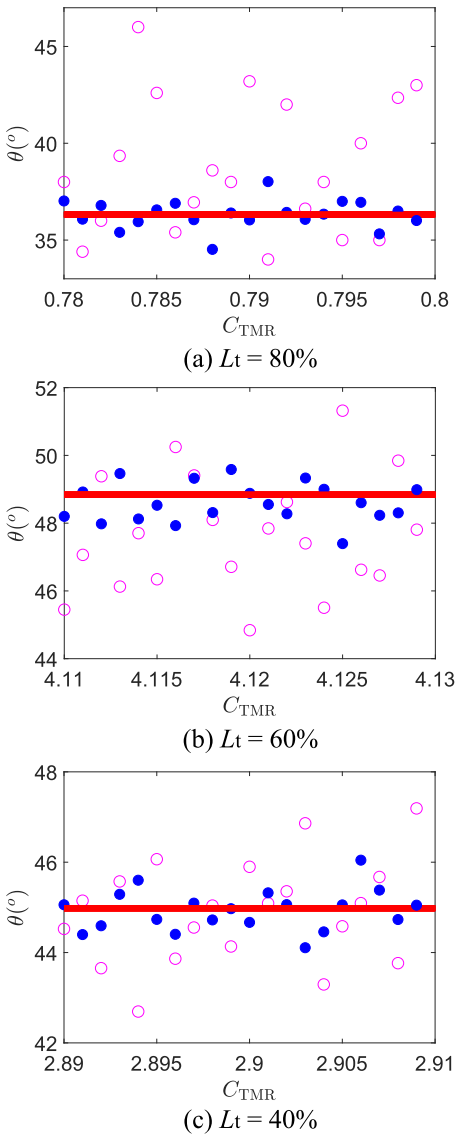

FIG. 9. Comparison of the predicted spray angle between the model with and without E_{SA}. The red lines indicate the experimental results. The blue point markers indicate the angle values predicted by the model with E_{SA}. The magenta circle markers indicate the ones predicted by the model without E_{SA}.

the background does not agree with the real target; the introduction of $\mathscr{L}_{E_{MC}}$ helps G identify the position and intensity of the droplet as well as the background shadow.

In the machine learning field, the parallel training usually is conducted with a batch form. Inputting a certain number of samples to the neural networks in a batch, the solutions are parallel generated and compared to the targets and an error is calculated. In our framework, when obtaining the predicted spray field, all the outputs, ten generated images, in one training batch will be averaged to one image. Then, this average image will be used to feed the down-sampling CNN to obtain the spray angle of this batch. To validate the spray angle estimator, we use the average images from experiments as test samples to output the angle values. Table II shows the comparison of spray angles obtained by *Manual Measurements* (MM) and CNN estimator. With the increase of C_{TMR}, the deviations between the two tend to be smaller. The error of all the test cases is less than 5.8%.

After this CNN estimator is trained, it only takes some milliseconds to output an angle value, which is according to the operating conditions of this batch. Then, the estimated value is employed in $\mathscr{L}_{E_{SA}}$ to update G. Due to the quick decrease at the beginning of the training, this error no longer affects G, only except for the abnormal generated solutions with angles diverged awfully from the theoretical model.

As shown in Fig. 9, the results predicted by the model without E_{SA} have large value ranges. The difference between maximum and minimum angles in a small momentum ratio level, $C_{TMR} \in [0.78, 0.80]$, even approach 12°. Meantime, the predicted angles have an "even-bias." Compared with the experimental measurements, all values are closer to the mean value of the whole domain. For small momentum ratios, as shown in Fig. 9(a), most of the predicted angle values are larger than the experimental results. For large momentum ratios, as shown in Fig. 9(b), most of the values are smaller than the experimental results. With the help of E_{SA}, this phenomenon is reduced and all three groups with different momentum ratios have the predicted angles closer to the experimental results. In addition, the predicted values of spray angles have narrower ranges.

B. Predictions

The literature showed that the macroscopic morphology study is important to characterize a spray.[46,47] Here, the simulated spray morphology is analyzed and compared with the experimental results.

Figure 10 compares the simulated and experimental spray morphology under different operating conditions. The typical spray morphology, i.e., liquid column formation, breakup of the column, and lateral expansion of the spray, can be clearly noted. The

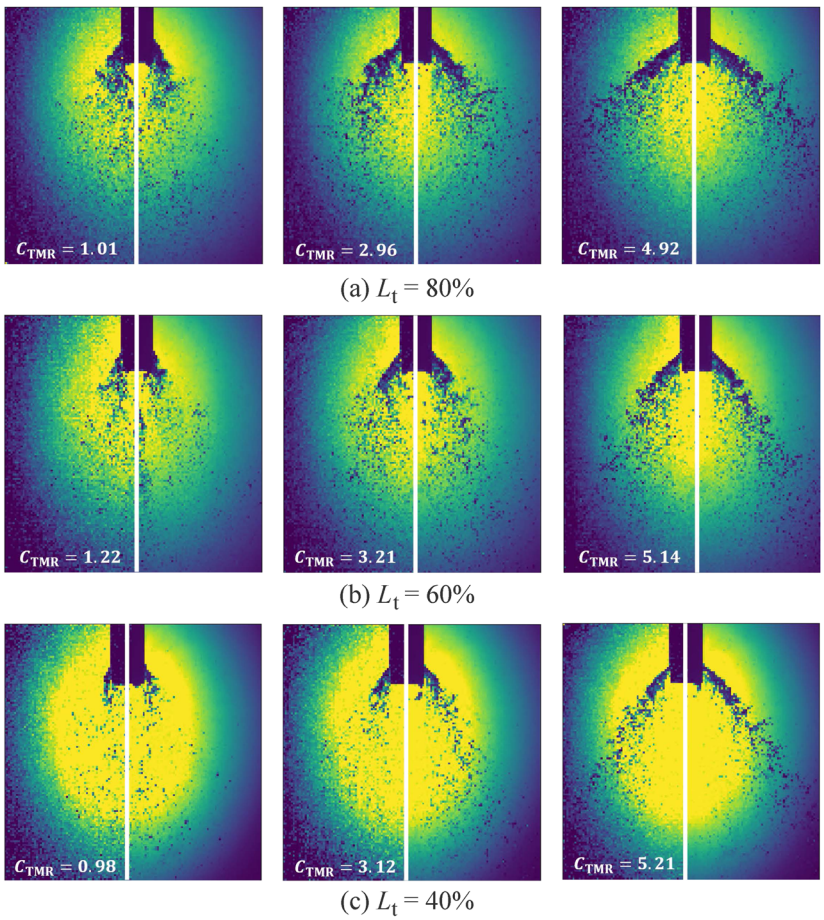

FIG. 10. Simulated and experimental spray morphology under different throttling levels and momentum ratios. The left half part is the simulated spray obtained by GAN-PE, and the right half part is the corresponding experimental high-speed image with the same size scale.

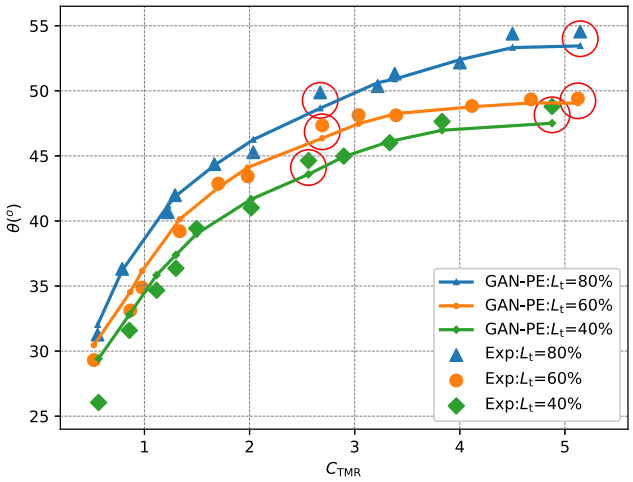

FIG. 11. The comparison of the spray angle between GAN-PE and experiments. The red circles show the cases that are out of the learning domain.

generated spray field shows that the droplets experience a size reduction before approaching a uniform tiny size distribution because of the impingement and collision. As shown in Fig. 10, the generated spray is fairly comparable with the experimental results; meanwhile, the hollow-cone-shaped profiles with a specific spray angle are well reproduced. For those cases that are out of the training domain, the last column in the figure, the generation also presents a similar good quality compared with those insides. Imperfectly, the background still represents grainy and the values of adjacent data points are not as continuous as those in the real images. However, all in all, the simulation succeeds to report the macroscopical morphology of the spray.

Figure 11 shows the curves of the spray angle vs momentum ratio at different throttling levels; it can be observed that the GAN-PE results coincide with the experimental results well in a wide momentum ratio range. According to theoretical analysis that has been explained in Sec. III C, the spray angle is mainly determined by the momentum ratio, and the simulated solutions also represent this. Due to the difficulties of E_{SA} to estimate the small angles, the predictions of the cases with small momentum ratios have relatively large errors. The values of different throttling levels are close to each other. For the test cases that are not in the learning domain, the results have a small deviation and all the predicted angle values are less than the manually measured ones. It is because these test cases are not constrained by the targets so the prediction has a trend to approach the mean value of the adjacent operating points, which is happened to be larger.

V. CONCLUSION

In this paper, we proposed a novel deep learning framework constrained by physical evaluators to directly predict spray solutions based on generative adversarial networks. The normal discriminator and the mass conservation and spray angle evaluators are used to constrain the CNN to generate the spray solution, including macroscopical morphology and spray angle. The former evaluator is able to improve the training convergence and the latter one helps to obtain more accurate spray angles that are consistent with the operating conditions. It is noteworthy that the related network architecture and spray problem are generic and the proposed framework is potentially suitable for other fluid field simulations that have proper prior physics knowledge. Further research will be carried out for spray droplet size analysis and prediction with the present network framework.

ACKNOWLEDGMENTS

This article was supported by the TUM Open Access Publishing Fund. Hao Ma was supported by the China Scholarship Council (Grant No. 201703170250). Chi Zhang was supported by Deutsche Forschungsgemeinschaft (Grant Nos. DFG HU1527/6-1 and DFG HU1527/10-1). The authors thank Xiangyu Hu, Nils Thuerey, Yujie Zhu, and Wei Wang for beneficial discussions and Anlong Yang for the experimental facilities.

DATA AVAILABILITY

The data that support the findings of this study are available from the corresponding author upon reasonable request.

REFERENCES

[1]G. Dressler and J. Bauer, "TRW pintle engine heritage and performance characteristics," in *36th AiAA/ASME/SAE/ASEE Joint Propulsion Conference and Exhibit* (AIAA, 2000), p. 3871.
[2]S. Heister, "Pintle injectors," in *Handbook of Atomization and Sprays* (Springer, 2011), pp. 647–655.
[3]K. Sakaki, H. Kakudo, S. Nakaya, M. Tsue, R. Kanai, K. Suzuki, T. Inagawa, and T. Hiraiwa, "Performance evaluation of rocket engine combustors using ethanol/liquid oxygen pintle injector," in *52nd AIAA/SAE/ASEE Joint Propulsion Conference* (AIAA, 2016), p. 5080.
[4]W. R. Hammock, Jr., E. C. Currie, and A. E. Fisher, "Apollo experience report: Descent propulsion system," NASA Technical Note D-7143 (1973).
[5]B. Bjelde, P. Capozzoli, and G. Shotwell, "The SpaceX Falcon 1 launch vehicle flight 3 results, future developments, and Falcon 9 evolution," in *59th International Astronautical Congress* (Space Exploration Technologies, 2008).
[6]M. J. Casiano, J. R. Hulka, and V. Yang, "Liquid-propellant rocket engine throttling: A comprehensive review," J. Propul. Power **26**, 897–923 (2010).
[7]K. Radhakrishnan, M. Son, K. Lee, and J. Koo, "Lagrangian approach to axisymmetric spray simulation of pintle injector for liquid rocket engines," Atomization Sprays **28**, 443–458 (2018).
[8]M. Son, K. Yu, K. Radhakrishnan, B. Shin, and J. Koo, "Verification on spray simulation of a pintle injector for liquid rocket engine," J. Therm. Sci. **25**, 90–96 (2016).
[9]M. Son, K. Radhakrishnan, Y. Yoon, and J. Koo, "Numerical study on the combustion characteristics of a fuel-centered pintle injector for methane rocket engines," Acta Astronaut. **135**, 139–149 (2017).
[10]J. Yu and J. S. Hesthaven, "Flowfield reconstruction method using artificial neural network," AIAA J. **57**, 482–498 (2019).
[11]H. Ma, Y.-x. Zhang, O. J. Haidn, N. Thuerey, and X.-y. Hu, "Supervised learning mixing characteristics of film cooling in a rocket combustor using convolutional neural networks," Acta Astronaut. **175**, 11–18 (2020).
[12]S. L. Brunton, B. R. Noack, and P. Koumoutsakos, "Machine learning for fluid mechanics," Annu. Rev. Fluid Mech. **52**, 477 (2019); arXiv:1905.11075v3.
[13]J. Ling, A. Kurzawski, and J. Templeton, "Reynolds averaged turbulence modelling using deep neural networks with embedded invariance," J. Fluid Mech. **807**, 155–166 (2016).
[14]E. J. Parish and K. Duraisamy, "A paradigm for data-driven predictive modeling using field inversion and machine learning," J. Comput. Phys. **305**, 758–774 (2016).

[15]K. Duraisamy, G. Iaccarino, and H. Xiao, "Turbulence modeling in the age of data," Annu. Rev. Fluid Mech. **51**, 357–377 (2019); arXiv:1804.00183v3.
[16]X. Jin, P. Cheng, W.-L. Chen, and H. Li, "Prediction model of velocity field around circular cylinder over various Reynolds numbers by fusion convolutional neural networks based on pressure on the cylinder," Phys. Fluids **30**, 047105 (2018).
[17]V. Sekar, Q. Jiang, C. Shu, and B. C. Khoo, "Fast flow field prediction over airfoils using deep learning approach," Phys. Fluids **31**, 057103 (2019).
[18]N. Omata and S. Shirayama, "A novel method of low-dimensional representation for temporal behavior of flow fields using deep autoencoder," AIP Adv. **9**, 015006 (2019).
[19]A. B. Farimani, J. Gomes, and V. S. Pande, "Deep learning the physics of transport phenomena," arXiv:1709.02432 (2017).
[20]M. D. Ribeiro, A. Rehman, S. Ahmed, and A. Dengel, "DeepCFD: Efficient steady-state laminar flow approximation with deep convolutional neural networks," arXiv:2004.08826 (2020).
[21]N. Thuerey, K. Weißenow, L. Prantl, and X. Hu, "Deep learning methods for Reynolds-averaged Navier–Stokes simulations of airfoil flows," AIAA J. **58**, 25–36 (2020).
[22]M. Raissi, P. Perdikaris, and G. E. Karniadakis, "Physics-informed neural networks: A deep learning framework for solving forward and inverse problems involving nonlinear partial differential equations," J. Comput. Phys. **378**, 686–707 (2019).
[23]M. Raissi, A. Yazdani, and G. E. Karniadakis, "Hidden fluid mechanics: Learning velocity and pressure fields from flow visualizations," Science **367**, 1026–1030 (2020).
[24]P. Holl, V. Koltun, and N. Thuerey, "Learning to control PDEs with differentiable physics," arXiv:2001.07457 (2020).
[25]L. Sun, H. Gao, S. Pan, and J.-X. Wang, "Surrogate modeling for fluid flows based on physics-constrained deep learning without simulation data," Comput. Methods Appl. Mech. Eng. **361**, 112732 (2020).
[26]L. Lu, X. Meng, Z. Mao, and G. E. Karniadakis, "DeepXDE: A deep learning library for solving differential equations," SIAM Review **63**, 208–228 (2021).
[27]H. Ma, X. Hu, Y. Zhang, N. Thuerey, and O. J. Haidn, "A combined data-driven and physics-driven method for steady heat conduction prediction using deep convolutional neural networks," arXiv:2005.08119 (2020).
[28]I. J. Goodfellow, J. Pouget-Abadie, M. Mirza, B. Xu, D. Warde-Farley, S. Ozair, A. Courville, and Y. Bengio, "Generative adversarial netowrks," arXiv:1406.2661.
[29]J. Kim and C. Lee, "Deep unsupervised learning of turbulence for inflow generation at various Reynolds numbers," J. Comput. Phys. **406**, 109216 (2020).
[30]J.-L. Wu, K. Kashinath, A. Albert, D. Chirila, H. Xiao *et al.*, "Enforcing statistical constraints in generative adversarial networks for modeling chaotic dynamical systems," J. Comput. Phys. **406**, 109209 (2020).
[31]M. Arjovsky, S. Chintala, and L. Bottou, "Wasserstein generative adversarial networks," in *International Conference on Machine Learning* (PMLR, 2017), pp. 214–223.
[32]K. Sakaki, H. Kakudo, S. Nakaya, M. Tsue, K. Suzuki, R. Kanai, T. Inagawa, and T. Hiraiwa, "Combustion characteristics of ethanol/liquid-oxygen rocket-engine combustor with planar pintle injector," J. Propul. Power **33**, 514–521 (2017).
[33]O. Ronneberger, P. Fischer, and T. Brox, "U-net: Convolutional networks for biomedical image segmentation," in *International Conference on Medical Image Computing and Computer-Assisted Intervention* (Springer, 2015), pp. 234–241.
[34]Z. Li, F. Liu, W. Yang, S. Peng, and J. Zhou, "A survey of convolutional neural networks: Analysis, applications, and prospects," in *IEEE Transactions on Neural Networks and Learning Systems* (IEEE, 2021).
[35]A. Khan, A. Sohail, U. Zahoora, and A. S. Qureshi, "A survey of the recent architectures of deep convolutional neural networks," Artif. Intell. Rev. **53**, 5455–5516 (2020).
[36]X. Mao, Q. Li, H. Xie, R. Y. Lau, Z. Wang, and S. Paul Smolley, "Least squares generative adversarial networks," in *Proceedings of the IEEE International Conference on Computer Vision* (IEEE, 2017), pp. 2794–2802.
[37]T. Karras, T. Aila, S. Laine, and J. Lehtinen, "Progressive growing of GANs for improved quality, stability, and variation," arXiv:1710.10196 (2017).
[38]M. Mirza and S. Osindero, "Conditional generative adversarial nets," arXiv:1411.1784 (2014).
[39]A. Paszke, S. Gross, F. Massa, A. Lerer, J. Bradbury, G. Chanan, T. Killeen, Z. Lin, N. Gimelshein, L. Antiga *et al.*, "PyTorch: An imperative style, high-performance deep learning library," arXiv:1912.01703.
[40]P.-K. Wu, K. A. Kirkendall, R. P. Fuller, and A. S. Nejad, "Breakup processes of liquid jets in subsonic crossflows," J. Propul. Power **13**, 64–73 (1997).
[41]J. Freeberg and J. Hogge, "Spray cone formation from pintle-type injector systems in liquid rocket engines," in *AIAA Scitech 2019 Forum* (AIAA, 2019), p. 0152.
[42]J. Yang, K. Zhang, H. Fan, Z. Huang, Y. Xiang, J. Yang, L. He, L. Zhang, Y. Yang, R. Li *et al.*, "Development and validation of deep learning algorithms for scoliosis screening using back images," Commun. Biol. **2**, 390 (2019).
[43]Y. Cai, L. Wang, M. Audette, G. Zheng, and S. Li, *Computational Methods and Clinical Applications for Spine Imaging* (Springer, 2020).
[44]H. Wu, C. Bailey, P. Rasoulinejad, and S. Li, "Automated comprehensive adolescent idiopathic scoliosis assessment using mvc-net," Med. Image Anal. **48**, 1–11 (2018).
[45]Y. Xie, E. Franz, M. Chu, and N. Thuerey, "tempoGAN: A temporally coherent, volumetric GAN for super-resolution fluid flow," ACM Trans. Graphics **37**, 1–15 (2018).
[46]M. Luo, "Experimental and numerical study of cryogenic flashing spray in spacecraft application," Ph.D. thesis, Technische Universität München, 2018.
[47]M. Luo, Y. Wu, and O. J. Haidn, "Temperature and size measurements of cryogenic spray droplets with global rainbow refractometry," J. Propul. Power **35**, 359–368 (2019).